Geometry of Curved Folded Developables

Seyon Mierunalan* and Keith A. Seffen†
University of Cambridge, Cambridge CP2 1PZ, United Kingdom

Origami inspired structures are gaining traction in the aerospace community. Often ignored, these structures exhibit an additional degree of freedom beyond rigid folding due to facet bending, leading to so called non-rigid Origami. A thin, initially plane *inextensible* sheet can be folded or creased along a general curve to form two concatenated *developable* surfaces that are not rigid or flat foldable. In the literature, theorems of differential geometry have been used to calculate the shape of a curved-line folded sheet by identifying kinematic constraints between the pair of developable surfaces. Two special cases; one in which the fold curve remains planar and the other in which the fold angle is constant, have been identified. In this work, we revisit these special cases through practical experiments and finite element analysis to quantify and validate the effectiveness of the analytical approach based on differential geometry. The results show excellent correlations with both elastic numerical modelling and differential geometry-based analysis able to capture the shape of the creased sheet influenced by crease rotation and facet bending. We then extend our methods to a special case of a curved creased disk and compare our predictions to experimental results. Agreement shows robustness and effectiveness of the differential geometric approach and also validates our numerical model, which may be applied to Origami structures with more complex extended curved crease networks.

I. Nomenclature

C	Crease curve
PG	Generator at point P on crease curve
s	Arc length of crease curve
$\kappa(s)$	Principal curvature of crease curve
$\tau(s)$	Twisting curvature of crease curve
κ_g	Principal curvature of crease curve
τ_g	Geodesic twisting curvature of crease curve
κ_N	Surface normal curvature of crease curve
κ_1	Major principal curvature
κ_2	Minor principal curvature
$\boldsymbol{t}, \boldsymbol{n}, \boldsymbol{b}$	Vector triad for crease curve in Euclidean space
$\boldsymbol{t}, \boldsymbol{u}, \boldsymbol{N}$	Vector triad for crease curve in local surface S_1
κ_1	Principal curvature of Surface S_1
γ	Orientation of κ_N & τ_g w.r.t PG
w	Half of crease angle
E	Young's modulus
ν	Poisson's ratio
θ	Orientation of an arbitrary generator
c	Principal curvature of internal region
a	Internal radius of circular disk
c_R	Principal curvature of rim region
β	Orientation of generators in rim region

II. Introduction

DESIGN of Origami inspired deployable space structures [1], micro-air vehicles [2], deployable stents [3] and tunable metamaterials [4] is made possible largely by mathematical methods that help understand Origami and associated folding and unfolding behaviour [5, 6]. Many of these structures are underpinned by motion localised within straight creases, albeit some that exhibit soft modes of deformation from facet bending [7]. This additional bending flexibility leads to non-rigid Origami, which has become of interest lately [8, 9]. Students of the Bauhaus Movement in the late 1920s discovered a variation of non-rigid Origami by folding along a curve [10]. Non-rigid folding enables curved creased structures to store elastic energy, with potential use in applications requiring actuation and deployability.

However in contemporary designs, applications of curved folded Origami are limited by a lack of understanding and require expertise in manufacturing techniques; some successful applications exist in the form of adaptive shading

*PhD Candidate, Advanced Structures Group, Department of Engineering, and AIAA Student Member.
†Professor of Engineering, Department of Engineering, and AIAA Senior Member

systems and fast-food containers. Material testing has also been done using timber [11] and aluminium [12], however, there is still a knowledge gap in how different materials perform for curved creased structures. Recently, there have been studies of curved crease Origami [13–17], but the question of how an arbitrary curved crease folds in 3D remains unanswered for the most part; in particular, a generic approach that can predict the shape of curved crease Origami with complex extended curved crease networks is largely absent.

In this work, we try to answer that question by revisiting the work of Duncan and Duncan [18]. In their paper, they identify a thin, initially plane *inextensible* sheet can be folded or creased along a general curve to form two concatenated *developable* surfaces that are not rigid or flat foldable. A developable surface is a smooth surface with zero Gaussian curvature everywhere, *i.e*. it is formed by bending or rolling of planar surfaces without need of stretching or tearing. Developable surfaces can be imagined to be ruled surfaces formed by tracing straight lines relative to a space curve; these straight lines are regarded as *generators*. The authors in Ref. [18] use theorems of differential geometry to calculate the shape of a curved-line folded sheet by identifying kinematic constraints between the pair of developable surfaces. Based on their experiments with sheet metal, two special cases are presented; one in which the fold curve remains planar and the other in which the fold angle is constant.

By understanding key features of curved creases through differential geometry and experiments, we propose a non-linear geometric elastic numerical model that can predict the geometry of curved crease Origami problems. The model is also capable of capturing hinge-like crease mechanics without need of a complex plastic material model. Following a review of fundamentals of differential geometry in Section III, we revisit special cases from Ref [18] through simple experimental models and a non-linear geometrical elastic model, to inspect the differential geometric approach in Section IV. We then study a simple problem of a closed curved crease inside a circular disk using differential geometry and reveal our proposed numerical model in Section V.

III. Curved Folded Developables

In this section, we review the fundamentals of differential geometry of curved folds and introduce the notation used throughout the paper while repeating the main details of Ref. [18] for completeness.

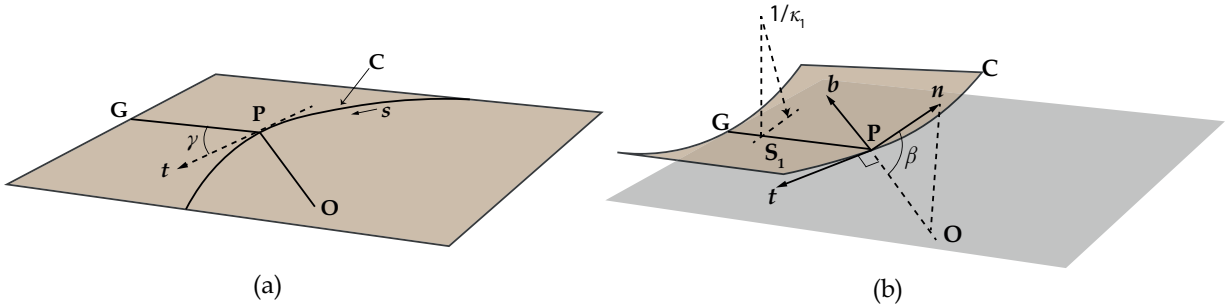

Fig. 1 A plane *inextensible* sheet divided into two regions by a fold curve, C. (a) The point P lies on the fold curve, C. PG is a generator of the surface in initial planar form. (b) Surface on the left of C deforms about the generator line PG to form *developable* surface S_1. The triad $\boldsymbol{t}$, $\boldsymbol{n}$, $\boldsymbol{b}$ is associated with the fold curve, C, which is now a twisted space curve [18].

Consider a curved crease line, C which divides part of a plane inextensible sheet into two regions as in Fig. 1(a). As a result, the sheet on the left hand side deforms into a developable surface with the generator PG. Now the curve, C is a twisted space curve which is associated with the moving triad $\boldsymbol{t}$, $\boldsymbol{n}$, $\boldsymbol{b}$ as shown in Fig. 1(b): $\boldsymbol{n}$ is the normal vector and $\boldsymbol{t}$ is the tangent vector and $\boldsymbol{b}$ is the binormal vector at a point P along the curve. The curve C may be specified by the principal curvature $\kappa(s)$ and torsion $\tau(s)$ of the curve, which are associated with the vector triad by Serret-Frenet formulae:

$$\begin{aligned} \mathrm{d}\boldsymbol{t}/\mathrm{d}s &= \kappa\boldsymbol{n} \\ \mathrm{d}\boldsymbol{n}/\mathrm{d}s &= -\kappa\boldsymbol{t} + \tau\boldsymbol{b} \\ \mathrm{d}\boldsymbol{b}/\mathrm{d}s &= -\tau\boldsymbol{n} \end{aligned} \tag{1}$$

This description is independent of any surface that contains the curve; however, these differential equations can be modified for the properties of the curve, C to read in terms of the properties of the surface S_1 with the aid of the triad $\boldsymbol{t}$, $\boldsymbol{u}$, $\boldsymbol{N}$, as illustrated in Fig. 2, given by Eq. 2:

$$\begin{aligned} \mathrm{d}\boldsymbol{t}/\mathrm{d}s &= \kappa_g \boldsymbol{u} + \kappa_N \boldsymbol{N} \\ \mathrm{d}\boldsymbol{u}/\mathrm{d}s &= -\kappa_g \boldsymbol{t} - \tau_g \boldsymbol{N} \\ \mathrm{d}\boldsymbol{N}/\mathrm{d}s &= -\kappa_N \boldsymbol{t} + \tau_g \boldsymbol{u} \end{aligned} \tag{2}$$

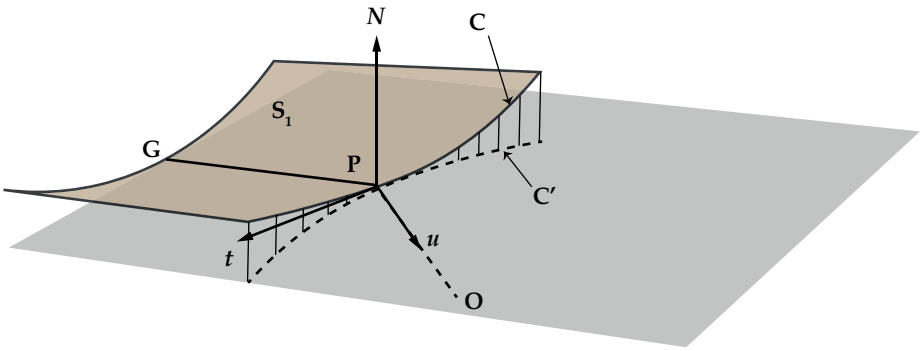

Fig. 2 Projection, C' of the fold curve, C on the tangent plane at P. The triad t, u, N is associated with the fold curve, C on the surface S_1.

The geodesic curvature, κ_g describes the original, planar layout of the fold curve and is a fixed property while normal curvature, κ_N correlates current surface curvature in a tangential direction to κ_g. The curvatures are related by Meusnier's theorem:

$$\kappa \boldsymbol{n} = \kappa_g \boldsymbol{u} + \kappa_N \boldsymbol{N} \tag{3}$$

This, in turn, formally relates these curvatures to the fold angle, $2w$ and ultimately to the spatial torsion of the fold curve, τ, the rate of change of fold angle along the curve, $\mathrm{d}w/\mathrm{d}s$ and to the corresponding geodesic torsion in the surface, τ_g, after the theorem of Bonnet, given by Eq. 4; a detailed derivation can be found in Ref. [18]:

$$\tau = \mathrm{d}w/\mathrm{d}s - \tau_g \tag{4}$$

These relations are used to determine the rules for compatible folding between the surfaces set by the conditions below:

$$\kappa_{N,2} = -\kappa_{N,1} \tag{5}$$

$$\mathrm{d}w_1/\mathrm{d}s = -\mathrm{d}w_2/\mathrm{d}s \tag{6}$$

where subscripts 1 and 2 correspond to surfaces 1 and 2 respectively. Equation 5 states that at any common point on the fold curve, surfaces have equal and opposite surface normal curvatures: as per Eq. 6, surfaces make equal fold angles to the local dihedral plane. The relationship between the geodesic torsions and the intrinsic variation of the fold angle along the curve then follows:

$$\tau_{g,2} = \tau_{g,1} - 2\mathrm{d}w_1/\mathrm{d}s \tag{7}$$

κ_N and τ_g, which are oriented at an arbitrary angle γ to the principal curvature κ_1 of the surface S_1, can be obtained by virtue of a Mohr's circle or Euler's formulae, which yield the following relationships:

$$\kappa_N = \kappa_1 \sin^2 \gamma \tag{8}$$

$$\tau_g = \kappa_1 \cos\gamma \sin\gamma \tag{9}$$

The fold angle, $2w$ at any point along the crease curve is then related to the spatial curvature of crease, κ and the surface normal curvature, κ_N, in Eq. 10:

$$\sin w = \kappa_g / \kappa \tag{10}$$

IV. Special Cases of Curved Folded Developables

Duncan and Duncan [18] illustrate two degenerate cases: Case I - where the folded curve lies in a plane and Case II - where the fold angle of the folded curve is the same everywhere, informed by their experiences of sheet-metal working. These conditions tend to be mutually exclusive, with a varying fold angle in the first case and an out-of-plane fold curve in the second. The geodesic torsion of both surfaces are shown to be equal and opposite in the first case and to be equal to each other in the second case where the fold angle is constant. Since the tangential curvatures are also known, by virtue of a Mohr's circle, the directions of pairs of generators linked across the fold curve are determined and the developable geometries of both surfaces on either side of the fold curve are completely specified in terms of their generators. For the first case, the authors show that the surface on one side is a mirror image in the osculating plane of the other; in other words, linked generators are collinear. In the second, the generators are analogous with light rays reflecting in planar optics *i.e.* equally inclined to the local tangent of the fold curve. In this section, we will study these two cases using simple physical models and a non-linear geometric numerical model implemented in commercial finite element package, `ABAQUS` [19], to test the validity.

A. Experimental Investigation

The generator directions remain unchanged during folding owing to the intrinsic nature of the Mohr's circle. Therefore, generators can be expressed simply in planar development - before folding occurs; we use this property to construct our physical models. Rectangular paper cards separated into two sections by a curved crease are marked with (a) collinear generators and (b) generators reflecting at equal angles about the curve in their planar form as illustrated in Fig. 3. The paper cards are then scored along the crease and the generators with a sharp scribe, to force them to deform into their corresponding shapes. Informal visual observations of the fold curve and fold angle in both cases confirm the predictions of the differential geometric approach. Observations also confirm that, in both cases, the curvatures of the linked generators are almost equal and opposite, giving locally concave and convex surfaces, cf. Section III.

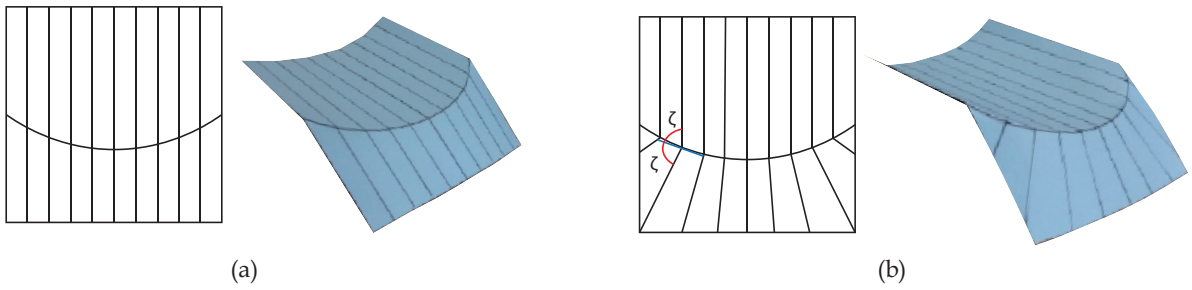

Fig. 3 Inextensible folding of paper card about straight generators and a fold curve of the two special cases of Duncan and Duncan [18] with planar development and deformed shape shown side-by-side. (a) The pairs of generators on either side of the fold are collinear in Case I and (b) equally inclined to the local tangent at a representative angle ζ in Case II. In both cases surfaces are curved in opposite senses on both sides. The fold curve in Case I remains planar but not in Case II, where the fold angle is constant.

B. Finite Element Analysis

Numerical models were developed in `ABAQUS` [19]. All models were considered to be made of a general linear-elastic material with Young's modulus, E = 105 GPa, Poisson's ratio, ν = 0.3, and a thickness, t = 0.1 mm. Note that the choice

of material properties should not affect the expected results, as the theoretical model based on differential geometry does not depend on material properties. Four-noded reduced integration shell elements (S4R) were used to create the plate mesh as they allow for large rotations under finite strains. The flat mesh was generated with constant thickness, and mesh sensitivity analysis was carried out for different creasing methods as discussed in Subsection 3 overleaf. The ABAQUS/Standard solver with Newton-Raphson time integration was used with non-linear geometry enabled.

1. Modelling Crease

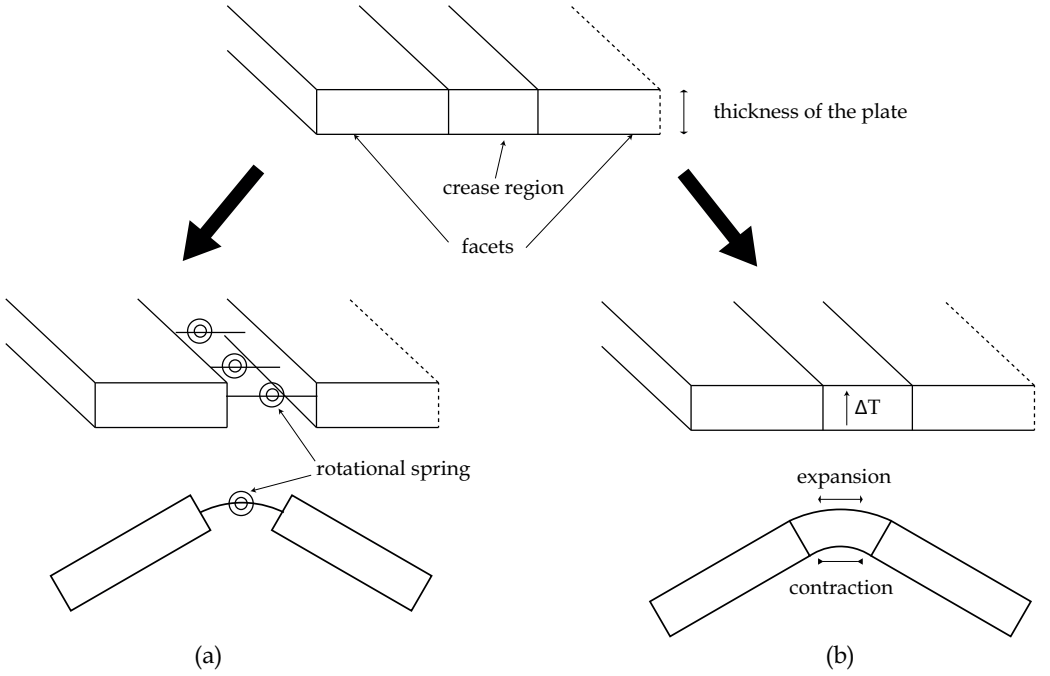

Fig. 4 Schematic of the crease modelling approaches employed in finite element analysis. (b) Connector approach: reference configuration (top), in which crease region is replaced with connector elements with rotational stiffness, and equilibrium configuration (bottom), after the plate has bent. (b) Temperature gradient approach: reference configuration (top), in which a thermal gradient, ΔT is applied through thickness along a narrow strip corresponding to the width of crease, and equilibrium configuration (bottom), after the plate has bent towards in the sense of the lower temperature, where the thermal gradient has induced curvature in the crease region.

Two different approaches, viz, [a] rotational hinges with predefined rotational stiffness and [b] thermal gradient field to induce hinge like creases, are employed to simulate creases, as illustrated in Fig. 4. In the first approach, the crease is considered singular where the plate is modelled as two distinct portions with collocated nodes at the crease boundary. The connection between two portions along the crease is established through connector elements and **COUPLING* constraint; a two-noded 3D connector element (CONN3D2) of *Join + Rotate* type is used. This particular type allows a single desired rotational degree of freedom between two points and rotational elasticity to account for rotational response of the crease, whilst translational degrees of freedom are constrained between the two edges for continuity of stress.

In the second approach, the crease is considered non-singular and twice the plate thickness wide informed by Ref. [20], and two options are possible: [b1] divide the plate into three parts; the narrow slice which is twice the plate thickness in width along the middle, corresponds to the crease, while the other two parts correspond to the facets either side. A thermal gradient, ΔT, is applied through the thickness of the plate. Only the crease region is allowed to expand by specifying a linear expansion coefficient in the narrow strip and zero elsewhere, and [b2] the temperature gradient, ΔT is specified through thickness of the plate along a set of nodes along the crease-line. The finite width of the crease is accounted for by ABAQUS by default, as the thermal gradient is automatically applied to the elements that share the selected nodes. The mesh required fine tuning to keep the size of the elements close to half the width of the crease

(which is equal to thickness of the plate [20]), close to the crease-line. In this option, the linear expansion coefficient is specified for the entire plate but only the elements that share the nodes to which thermal gradient is applied will undergo expansion.

2. Boundary Conditions

In the connector approach, when simulating crease with constant angle throughout, the rotational behaviour is uniformly distributed along the fold-line using **COUPLING* constraint with kinematic coupling. However in the case of varying crease angle, a finite number of connector elements are used, and the angular displacement is specified for each connector element based on the relationship given in Eq. 10. To maintain the planar nature of crease in the latter, vertical displacement of the nodes along crease is restrained.

In the temperature gradient approach, when modelling the crease with constant angle throughout, the same temperature gradient is specified for all nodes along the crease. In the case of varying crease angle, the temperature gradient is varied along the crease based on the relationship given in Eq. 10.

3. Mesh Sensitivity

Case I, where the fold-line remains, planar is used to perform convergence study on mesh discretisation. Measuring the fold-angle in the case of temperature gradient approach is not straightforward as the crease is non singular and presents problems with defining tangent lines in order to measure angles. Hence, the vertical displacement of the free edge on concave side of the crease is considered for the mesh sensitivity analysis. A non-uniform mesh was created with a finer mesh close to the crease and increasingly coarser towards the free edges. Therefore, in order to make a meaningful comparison, the size of the elements close to the crease as a ratio of plate thickness (t) is considered. The vertical displacement of the centre of the free edge on concave side of the crease versus the relative size of the element close to the crease is presented in Fig. 5. It can be seen that the connector approach (method [a]) produces constant vertical displacement over the range of element sizes considered: this is expected, as this approach is capable of producing sharp curvature changes regardless of the element size. In the temperature approach method [b1], the vertical displacement reaches an almost consistent value after a relative size of $t/11$. Method [b2] runs into numerical instabilities if elements are discretised beyond $t/3$, and is unable to achieve the full range of displacement. Note that all simulations were performed keeping the temperature gradient, ΔT, constant at 8×10^8 °C / m. This is the largest temperature gradient possible for the range of element sizes considered before encountering numerical instabilities.

4. Results and Discussion

Figure 6 shows the deformed shape obtained from finite element analyses: Fig 6(a) for the connector approach and Fig. 6(b) for the temperature approach. The former closely resembles the shapes obtained from experiments with cylindrical deformation on both sides in Case I and cylindrical and conical deformations in Case II; which we will confirm quantitatively shortly. However, in the latter approach, method of splitting the plate into three regions and specifying the temperature gradient to the narrow middle strip, Fig. 6(b1), produces similar shapes to that of experiments and connector based models. However, the method of specifying the temperature gradient along the centre-line of the plate, Fig. 6(b2), suffers from localised deformations and non-convergence, and is unable to achieve the full range of displacement. The reason is because only one element on either side of the selected nodes undergo expansion and is unable to achieve high enough curvature beyond a certain limit, leading to numerical instability. This problem is not present in method [b1] as the crease region is discretised finer.

Both method [a] and [b1] offer similar deformed shapes but have different functional advantages and disadvantages when used to model creases in finite element analyses. Method [a] is well suited to capturing a known dihedral angle and produces well controlled shapes. However, if the structure is to be loaded after it is deformed via method [a], the fold-angle would remain fixed, which is unrealistic. This can be alleviated by specifying angular moments instead of angular displacements during deformation. Method [b1] is useful in metal forming simulations and in studying intrinsic nature of creases; however, it is computationally more expensive than method [a], and modelling multiple creases using this method is cumbersome e.g. specifying the dihedral angle is not straightforward as the relationship between fold-angle and temperature gradient should be established first. In this method, the crease region can be made softer or highly expandable by finetuning material properties of the crease region alone, to account for stiffness of the crease, which is achieved by means of the rotational spring stiffness in method [a].

We will now make a quantitative comparison of finite element results with the predictions from the differential

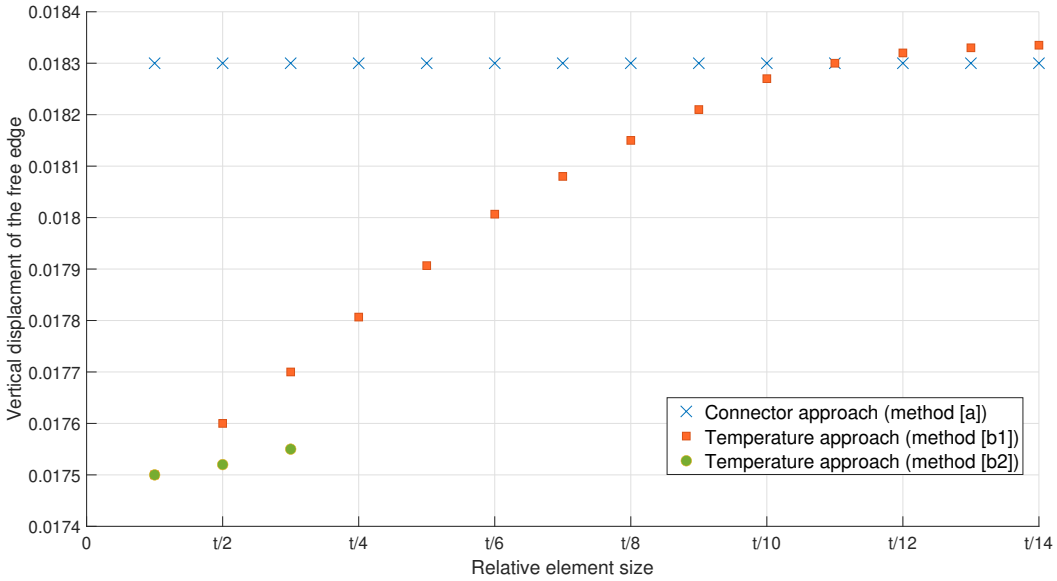

Fig. 5 Convergence study on shell discretization. Vertical displacement of the centre of free edge on the concave side of the crease is plotted against the smallest element size as a ratio of plate thickness, t. Connector approach (method [a]) produces constant vertical displacement over the range of element sizes considered. In the temperature approach method [b1], the vertical displacement reaches an almost consistent value after a relative size of $t/11$. Method [b2] encounters numerical instabilities beyond $t/3$. The connector approach is the most computationally efficient of the three methods.

geometric approach; only the results from the connector approach are considered. To this end, we find principal curvatures from the finite element results and convert them into generator plots. First, the curvatures, κ_x and κ_y, and twisting curvature, κ_{xy} of the plate, are written at every node in a local (x, y) coordinate system oriented at an angle χ to the principal curvature direction from `ABAQUS`. A spectral decomposition of this symmetric matrix produces diagonal components of the new matrix, which returns its eigenvalues, corresponding to principal curvatures, while their directions are represented by eigenvectors. The principal curvatures, κ_1 and κ_2 and corresponding directions, χ are thus calculated at every node, and their principal curvature directions can be plotted as directional lines at each node.

Figure 7 shows the major principal curvature direction plots for both cases.. The finite element results remarkably match the predictions from the differential geometric approach; with collinear generators in Case I and generators reflecting at equal angle about the tangent in Case II. Finite element analysis captures the 'free edge' boundary condition, where the plate does not achieve pure cylindrical/conical deformation at the unsupported edges (which is absent in the differential geometric approach). Nevertheless, the results confirm the validity of the differential geometric approach for predicting the shape of curved creased structures. In the next section, we will study a generic problem to test both the differential geometric approach and our non-linear geometric finite element analysis.

V. Circular Disk with Closed Circular Crease

A curved "open" crease runs from edge-to-edge as in the previous cases; a "closed" crease is entirely contained inside the plate. To understand the deformation of closed shells with closed creases, we take a basic problem: a flat circular disk with a single central circular crease. In this section, we extend the differential geometric approach based on Ref. [18] to predict the geometry of the creased disk, informed by experimental and numerical investigations.

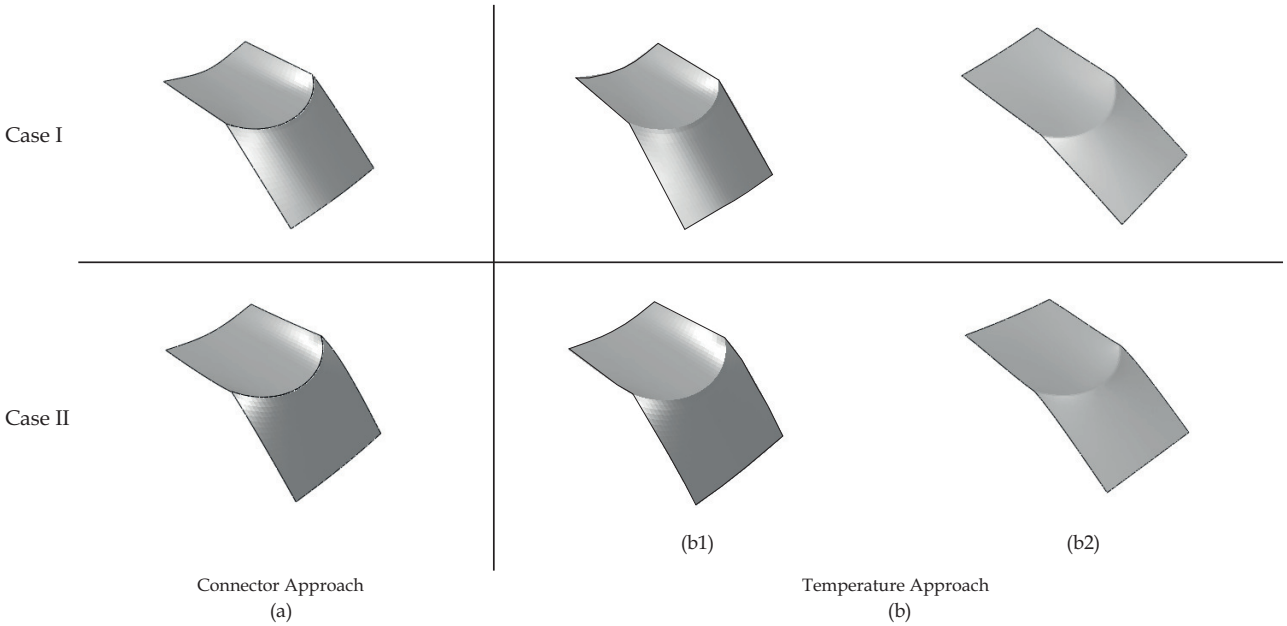

Fig. 6 Deformed shape obtained from finite element analyses of special cases from Duncan and Duncan [18]. (a) Using our "connector approach", close resemblance to the shapes obtained from experiments is achieved, with cylindrical deformation on both sides in Case I (left) and cylindrical and conical deformations in Case II (right). (b) Using our "temperature approach": (b1) similar shape to that of experiments and connector based model is achieved, but (b2) models suffer from localised deformations and non convergence, and is unable to achieve the full range of displacement as the other models.

A. Experimental Investigation

Disks with a diameter of 80 mm were cut from shim steel sheets of varying thickness using a water jet cutter, in order to minimise initial stresses and bends on the edges, and for a higher degree of accuracy and precision. Choosing 80 mm affords a disk that is easy to crease, handle and observe.

1. Scoring

The generic method of forming creases in thin sheets is scoring by hand with a pointed object along a known path. In experiments, using a ball-point pen and a stencil, circular creases are scribed onto the disks using approximately the same pressure. Application of same pressure is somewhat subjective, however with practice it was achieved to a greater extent, forming a constant fold-angle across the crease. Alternatively, using a steel indenter, a circular crease can be imprinted on circular disks with Instron machine.

2. Observations

Upon scoring, the disk deforms out of plane into a general saddle shape. The deformation was primarily cylindrical inside the crease region and conical in the rim region. Other interesting features are the two 'dead zones', characterised by sharp cone like deformation at the top and bottom of the rim region as shown in Fig. 8(a).

When indented by Instron instead, the disk deforms irregularly with petal like formations in the outer rim region, characterised by wave like deformation as shown in Fig. 8(c); the deformation was partially cylindrical inside the crease region. Such deformation arises from indenting process, where the disk deforms instantaneously rather than progressively. The experiments were repeated for several specimens and different thickness and similar observations were made. Since differential geometric approach is only applicable to developable deformations, only the case of creasing with a ball-point pen is relevant for differential geometric approach.

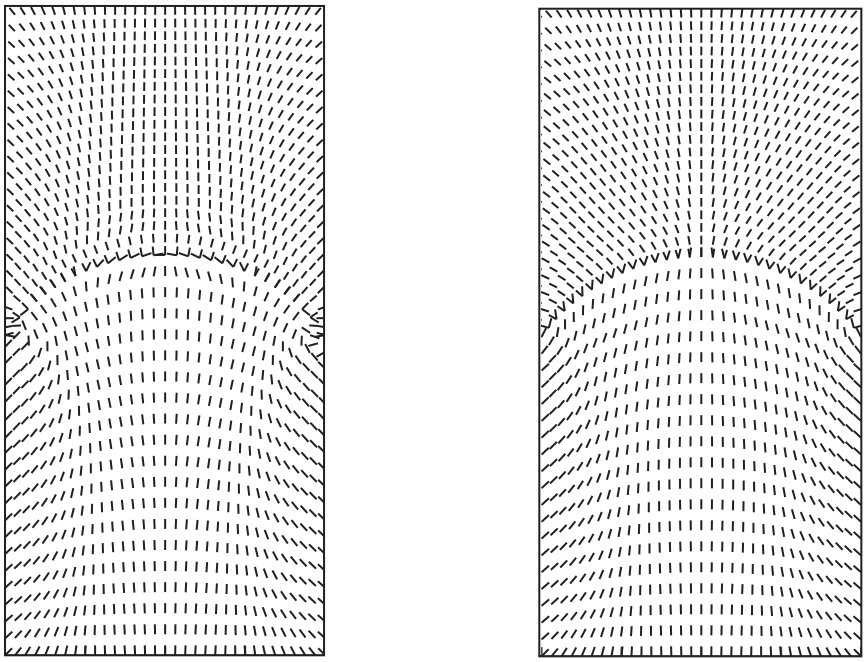

(a) (b)

Fig. 7 Plot of major principal curvature direction at each node of finite element analyses of Duncan and Duncan [18] special cases. (a) Case I - where the crease-line is planar. (b) Case II - where the crease has equal angle throughout. Black straight lines indicate the major principal curvature direction at each node: connecting adjacent nodes with black lines in the same direction produces generators of the sheet. Generators match the predictions from the differential geometric approach with collinear generators in Case I and generators reflecting at equal angle about tangent in Case II with the 'free edge' boundary condition evident, where the plate has not achieved pure cylindrical/conical deformation at the unsupported edges.

B. Differential Geometric Approach

This section extends the work of Duncan and Duncan [18] in predicting the shape of the circular creased sheets. Experiments shed some light on the shape of the internal region enclosed by the fold-line to be approximately cylindrical: therefore let the constant curvature of the entire internal region (κ_1) be c. Following notation in Section III, the internal properties of the curved disk are described below.

An arbitrary internal generator which makes an angle θ with the principal curvature axis through the centre and the fold-line, is inclined at an angle γ with the tangent to the fold-line, as illustrated in Fig. 9. Thus:

$$\gamma = \frac{\pi}{2} - \theta \tag{11}$$

The shell curvature on the fold-line of the internal region (denoted by suffix i) is therefore given by Eq. 8:

$$\kappa_{N,i} = \kappa_1 \sin^2 \gamma \tag{12}$$

and from Eq. 11,

$$\kappa_{N,i} = c \cos^2 \theta \tag{13}$$

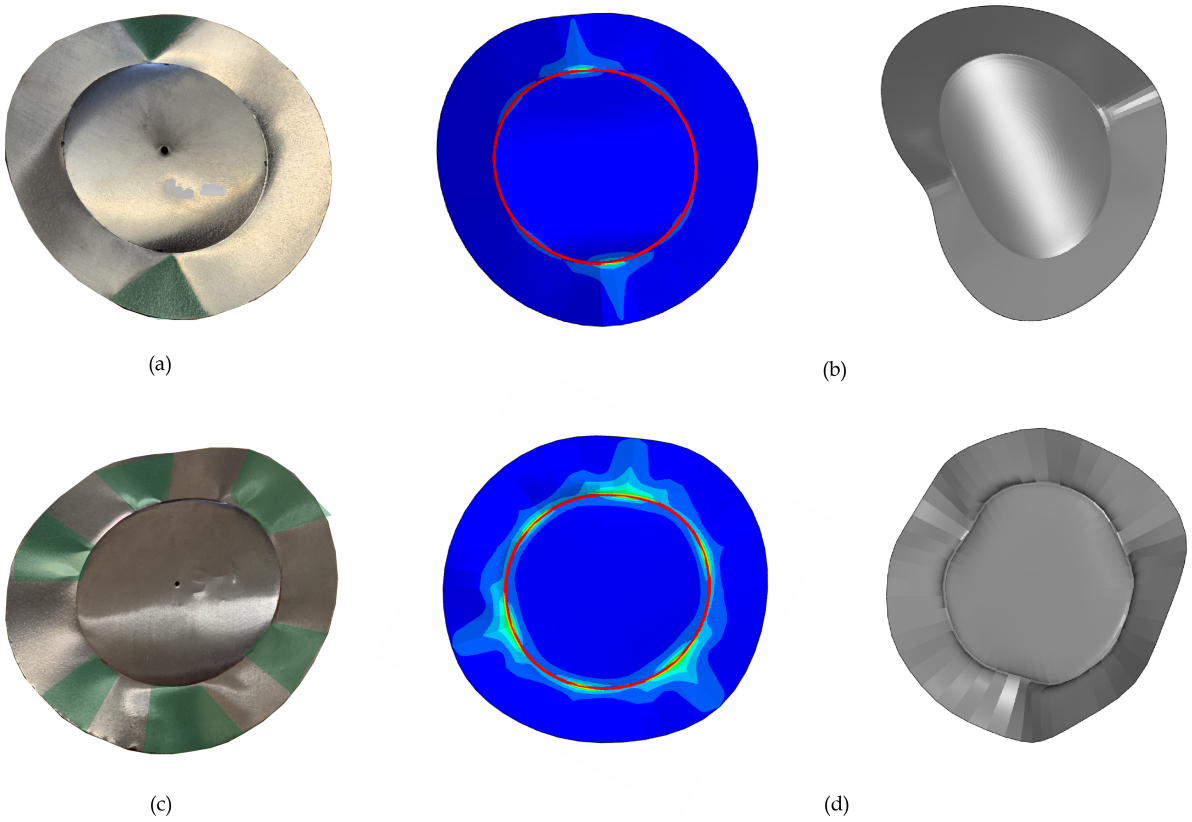

Fig. 8 Comparison of deformed circular discs with Finite Element analyses. (a) When scored with a ball-point pen, the disk deforms out of plane into a saddle shape; with cylindrical deformation in the internal region within the crease and conical deformation in the outer rim region. Two 'dead zones', characterised by sharp cone like deformation are at the top and bottom in the rim region, overlaid in green in the figure. (b) Finite Element Analysis of a circular disk scored by introducing a thermal gradient along the circular crease-line sequentially, there is a remarkably similar shape to the actual specimen scored by a ball point pen. The disk deforms out of plane into a saddle shape, with cylindrical deformation in the internal region within the crease and conical deformation in the rim region, with two dead zones. A similar shape is obtained using the connector approach as well. (c) When indented with a circular steel indenter, the disk deforms irregularly, with several petal like formations in the outer rim region and some cylindrical deformation in the internal region. (d) Finite Element Analysis of a circular disk scored by introducing thermal gradient all at once along the circular crease-line produced close results to that of the actual specimen with six dead zones. The connector approach failed to converge to a solution.

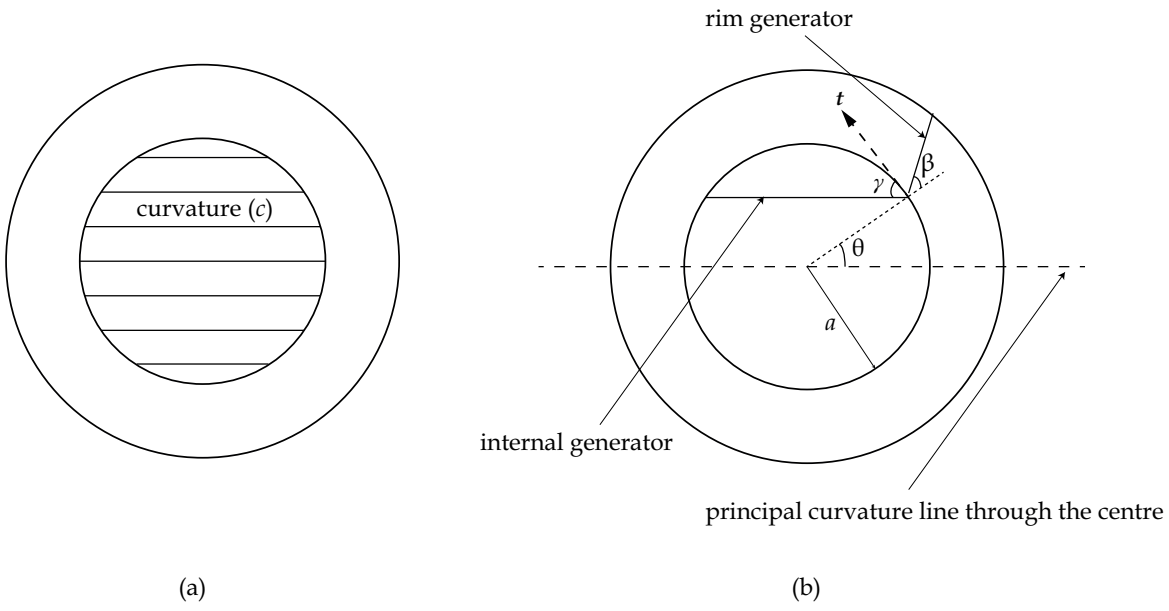

Fig. 9 Problem definition for the analytical model. (a) The internal region of the circular disk imprinted with a central circular crease of radius, a, attains a cylindrical deformation, thus acquiring a constant maximum principal curvature, c throughout. It is characterised by a generator profile consisting of parallel lines as shown. (b) An arbitrary internal generator subtending an angle θ with the principal curvature line through the centre as shown deviates by β to form a generator line of the external rim region.

The geodesic torsion, $\tau_{g,i}$, is equivalent to the surface twist rate, given by

$$\tau_{g,i} = \frac{1}{2}(-\kappa_1)\sin 2\gamma = -\frac{c}{2}\sin(2\theta - \pi) = c\sin\theta\cos\theta \tag{14}$$

Thus, on the fold-line, the cylindrical curved surface has local shell curvature and geodesic torsion as $\kappa_{N,i}$ and $\tau_{g,i}$ given by Eqs 13 & 14. From Bonnet's Theorem, the developable folding conditions require, for both surfaces, inside (i) and outside (o) the crease to obey:

$$\frac{dw}{ds} = (\kappa_g \kappa_N' - \kappa_N \kappa_g')/\kappa^2 \tag{15}$$

where $w_{i,o}$ are respective normal angles and κ_g is the geodesic fold curvature.

Two other conditions must also be satisfied for compatible folding, as discussed in Section III. The first condition being that the surfaces should have equal and opposite surface normal curvatures along the fold-line:

$$\kappa_{N,o} = -\kappa_{N,i} \tag{16}$$

and the second being the relationship between inside and outside geodesic torsion:

$$\tau_{g,o} = \tau_{g,i} - 2\frac{dw_i}{ds} \tag{17}$$

Hence the generators of the outside region can be constructed by determining $\kappa_{N,o}$ and $\tau_{g,o}$ from the relationships given by Eqs 16 & 17 and constructing a Mohr's circle. Determining $\kappa_{N,o}$ is straightforward from Eqs 13 & 16, which yield:

$$\kappa_{N,o} = -c\cos^2\theta \tag{18}$$

The geodesic curvature of fold-line is simply its original curvature, $\kappa_g = 1/a$. Hence, $d\kappa_g/ds = 0$ and $s = a\theta \Rightarrow d/ds = (1/a)d/d\theta$. From these relationships,

$$\kappa'_{N,i} = \frac{1}{a}\frac{d}{d\theta}(c\cos^2\theta) = -2\frac{c}{a}\cos\theta\sin\theta \tag{19}$$

From combining Eqs 13, 15 & 19:

$$\frac{dw_i}{ds} = (\kappa_g\kappa'_{N,i})/(\kappa_g^2 + \kappa_{N,i}^2) = \frac{-2c\cos\theta\sin\theta}{1 + a^2c^2\cos^4\theta} \tag{20}$$

Substituting into Eq. 17 yields,

$$\tau_{g,o} = c\cos\theta\sin\theta\left[1 + \frac{4}{1 + a^2c^2\cos^4\theta}\right] \tag{21}$$

From these results, the Mohr's circle at an arbitrary point along the fold-line can be constructed for inside and outside surfaces in Fig. 10.

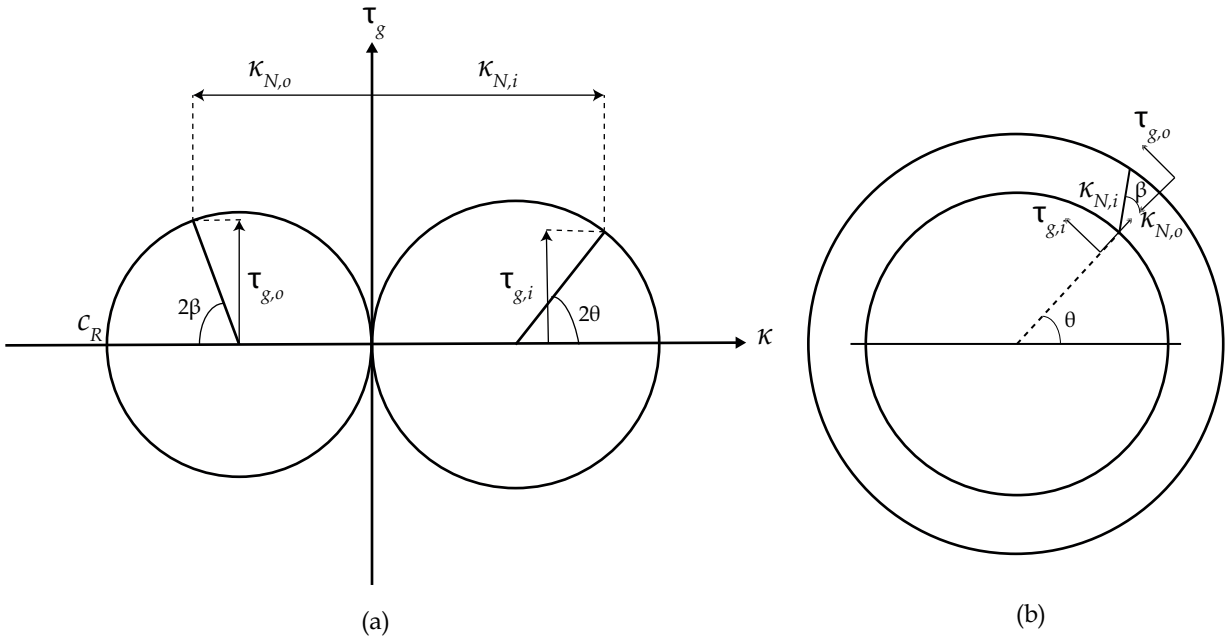

Fig. 10 (a) Mohr's circle diagram showing the relationship between normal curvature (K_N) and geodesic torsion (τ_g) for both inside (i) and outside (o) region of a circular disk with single central circular crease. c_R is the generator rim curvature at a given point. (b) Planar development of the circular disk with single central circular crease. On the fold-line, the cylindrical curved inside surface has local shell curvature and geodesic torsion, $\kappa_{N,i}$ and $\tau_{g,i}$ and the conical outside region has local shell curvature and geodesic torsion, $\kappa_{N,o}$ and $\tau_{g,o}$.

From the geometry of the Mohr's circle, we see that:

$$c_R/2[1 + \cos 2\beta] = c\cos^2\theta = c_R\cos^2\beta \tag{22}$$

and:

$$c_R/2\sin 2\beta = \tau_{g,o} = c_R\sin\beta\cos\beta \tag{23}$$

where c_R is the principal curvature of the rim region. From Eqs 22 & 23:

$$\frac{c_R\sin\beta\cos\beta}{c_R cos^2\beta} = \frac{\tau_{g,o}}{c\cos^2\theta} \tag{24}$$

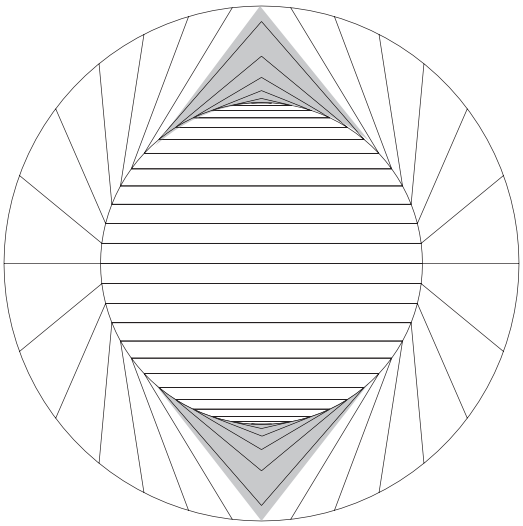

Fig. 11 Generator profile of an 80 mm diameter disk with a single central circular crease of 50 mm diameter as predicted by Eq. 25 derived from differential geometry. In the regions highlighted in grey, the differential geometric approach predicts intersecting generators, which is not possible for developable deformation. The location of such regions is consistent with the two dead zones observed in the physical model.

Equation 24 now reduces to

$$\tan\beta = \tan\theta\left[1 + \frac{4}{1 + (ac)^2\cos^4\theta}\right] \tag{25}$$

Equation 25 constitutes the generator profile of the rim region and depends on the internal radius a, curvature of the internal region c and inclination of a generator to the principal curvature line through the circle centre, θ: Figure 11 shows the generator profile plotted from Eq. 25.

The model predicts two zones in which the generator lines intersect, highlighted in Fig. 11. Generator lines cannot intersect if the surface is developable; hence, these two regions correspond to the earlier 'dead zones' in the actual specimen scored with a ball-point pen.

C. Finite Element Analysis

The finite element model formulated from Section IV is used to set-up numerical models of circular disks in `ABAQUS` [19], where both method [a] and method [b1] are used to model the crease. To mimic the experimental and analytical models, the crease is modelled with varying angle around the crease based on the relationship given in Eq. 10. Both methods were able to produce the shape that resembled the experimental observation from creasing with a ball-point pen. The earlier Fig. 8(b) shows the deformed shape of the disk. an attempt was also made to simulate instantaneous creasing via the Instron machine using both methods. The crease was restrained against vertical displacement, and an equal dihedral angle was specified along the crease. However, the connector approach failed to converge while the temperature approach (b1) produced results that closely resemble the experimental observation, Fig. 8(d). The connector approach effectively overconstrains the crease during analysis, which has to be resolved in order to converge to a solution.

To make a quantitative comparison, a similar approach to Section IV is adopted where the generator profile is produced from finite element data, see Fig. 12(a): there is a remarkable resemblance to analytical results, but there are some locations close to the crease which deviate from theoretical behaviour. The Gaussian curvature, product of principal curvatures is an indicator of non-developable behaviour, plotted in Fig. 12(b). Zero Gaussian curvature

indicates that one of the two principal curvatures is zero, thus informing developable deformation in the disk. As it can be seen, the plot reveals that the Gaussian curvature is zero everywhere except for certain regions close to the crease, where deviation of generator profile is also observed. Locations with non-zero Gaussian curvature will not obey folding conditions set out by the differential geometric approach, which has the inherent developable deformation assumption. The concentration of Gaussian curvature at four locations in the disk is consistent with the four-vertex theorem for closed convex space curve, where there are four points with vanishing torsion or extreme curvature [21]; similar four locations were determined analytically in Ref. [13] for an annulus. Overall, differential geometric approach though it predicts the overall geometry of closed creased structure to a fair accuracy, it fails to capture the intrinsic deviations, which is better captured by the numerical models discussed in this paper.

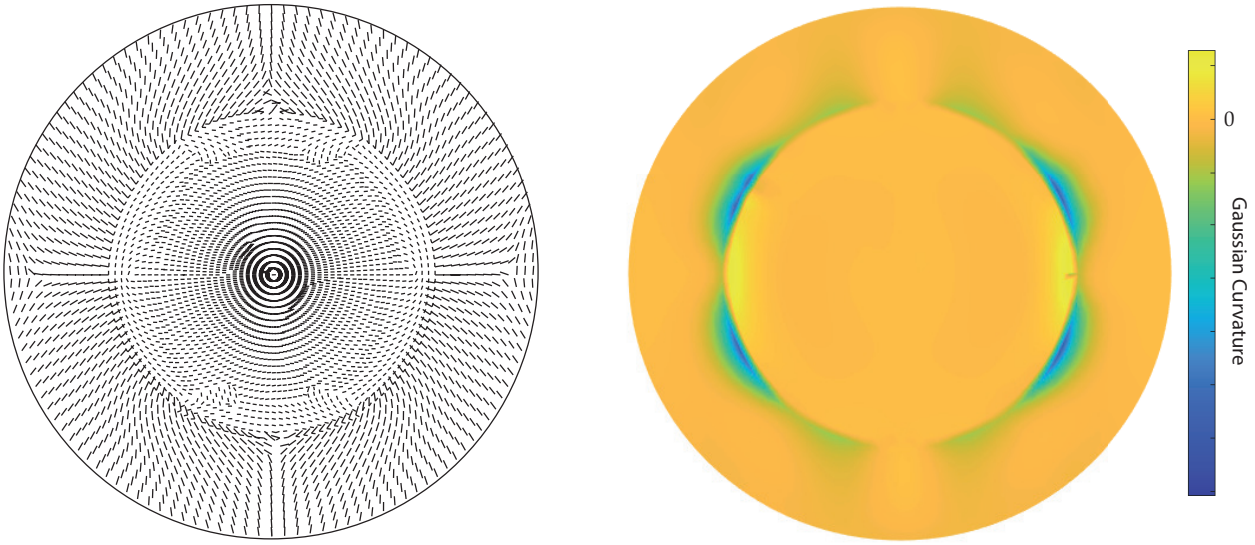

(a) (b)

Fig. 12 Results from finite element analysis of a creased circular disk. (a) Plot of major principal curvature direction at each node. Black straight lines indicate the major principal curvature direction at each node. Connecting adjacent nodes with black lines in the same direction produces generators of the sheet. The profile agrees with analytical prediction for the most part except for regions close to the crease. (b) Plot of Gaussian curvature ($\kappa_1\kappa_2$); zero values indicates developable deformation of the disk, almost everywhere except at regions close to the crease.

VI. Concluding Remarks

This study was aimed at the geometry of curved crease structures through non-linear geometric finite element analysis, validated by practical experiments and an analytical method based on differential geometry. To this end, two different problems were considered: a rectangular sheet with an open curved crease that runs from edge to edge, and a circular sheet with a closed circular crease. Three different methods were employed to implement creases in finite element models, and each method has its functional advantages and disadvantages which should be considered when using them to model curved creases. For example, the connector method was more computationally efficient in modelling a rectangular sheet with an open curved crease, while the temperature method of segmenting the plate into crease and facets proved effective in modelling a circular sheet with a closed circular crease. The finite element results show excellent correlation between experimentally and analytically determined shapes, while also capturing intrinsic features like 'free edge' boundary condition in the case of a rectangular sheet with an open crease, and four locations of extreme curvature in the case of a circular sheet with a closed crease. This paper is primarily based on simple, single curved creases, but the numerical model will be useful for the design and analysis of Origami structures with more complex extended curved crease networks.

VII. Acknowledgements

SM is grateful for Schlumburger Cambridge International Scholarship from the Cambridge Commonwealth, European, and International Trust for PhD study at the University of Cambridge.

References

[1] Miura, K., "Concepts of deployable space structures," *International Journal of Space Structures*, 1993. https://doi.org/10.1177/0266351193008001-202.

[2] Nakata, T., Liu, H., Tanaka, Y., Nishihashi, N., Wang, X., and Sato, A., "Aerodynamics of a bio-inspired flexible flapping-wing micro air vehicle," *Bioinspiration and Biomimetics*, 2011. https://doi.org/10.1088/1748-3182/6/4/045002.

[3] Lipton, J. I., MacCurdy, R., Manchester, Z., Chin, L., Cellucci, D., and Rus, D., "Handedness in shearing auxetics creates rigid and compliant structures," *Science*, 2018. https://doi.org/10.1126/science.aar4586.

[4] Hawkes, E., An, B., Benbernou, N. M., Tanaka, H., Kim, S., Demaine, E. D., Rus, D., and Wood, R. J., "Programmable matter by folding," *Proceedings of the National Academy of Sciences of the United States of America*, 2010. https://doi.org/10.1073/pnas.0914069107.

[5] Maekawa, J., and Kasahara, K., *Viva Origami! (in Japanese)*, Sanrio Publications, Tokyo, 1983.

[6] Kawasaki, T., "On the relation between mountain-creases and valley-creases of a flat Origami," Tech. rep., Sasebo College of Technology Report, 1990.

[7] Silverberg, J. L., Na, J.-H., Evans, A. A., Liu, B., Hull, T. C., Santangelo, C. D., Lang, R. J., Hayward, R. C., and Cohen, I., "Origami structures with a critical transition to bistability arising from hidden degrees of freedom," *Nature Materials*, Vol. 14 (4), 2015, pp. 389–393. https://doi.org/10.1038/nmat4232.

[8] Liu, K., and Paulino, G. H., "Nonlinear mechanics of non-rigid Origami: An efficient computational approach," *Proceedings of the Royal Society A: Mathematical, Physical and Engineering Sciences*, 2017. https://doi.org/10.1098/rspa.2017.0348.

[9] Andrade-Silva, I., Adda-Bedia, M., and Dias, M. A., "Foldable cones as a framework for nonrigid origami," *Physical Review E*, Vol. 100, 2019, p. 033003. https://doi.org/10.1103/PhysRevE.100.033003.

[10] Demaine, E. D., Demaine, M. L., Koschitz, D., and Tachi, T., "Curved crease folding: a review on art, design and mathematics," *Proceedings of the IABSE-IASS Symposium: Taller, Longer, Lighter (IABSE-IASS2011)*, 2011.

[11] Buri, H., Stotz, I., and Weinand, Y., "Curved folded plate timber structures," *IABSE-IASS Symposium*, 2011.

[12] Eversmann, P., Ehret, P., and Ihde, A., "Curved-folding of thin aluminium plates: towards structural multi-panel shells," *Proceedings of the IASS Annual Symposium 2017 "Interfaces: architecture.engineering.science"*, 2017.

[13] Dias, M. A., Dudte, L. H., Mahadevan, L., and Santangelo, C. D., "Geometric mechanics of curved crease origami," *Physical Review Letters*, 2012. https://doi.org/10.1103/PhysRevLett.109.114301.

[14] Vergauwen, A., Laet, L. D., and Temmerman, N. D., "Computational modelling methods for pliable structures based on curved-line folding," *CAD Computer Aided Design*, 2017. https://doi.org/10.1016/j.cad.2016.10.002.

[15] Lee, T. U., You, Z., and Gattas, J. M., "Elastica surface generation of curved-crease origami," *International Journal of Solids and Structures*, 2018. https://doi.org/10.1016/j.ijsolstr.2017.11.029.

[16] Badger, J. C., Nelson, T. G., Lang, R. J., Halverson, D. M., and Howell, L. L., "Normalized coordinate equations and an energy method for predicting natural curved-fold configurations," *Journal of Applied Mechanics, Transactions ASME*, 2019. https://doi.org/10.1115/1.4043285.

[17] Woodruff, S. R., and Filipov, E. T., "A bar and hinge model formulation for structural analysis of curved-crease Origami," *International Journal of Solids and Structures*, 2020. https://doi.org/10.1016/j.ijsolstr.2020.08.010.

[18] Duncan, J. P., and Duncan, J. L., "Folded developables," *Proceedings of the Royal Society A: Mathematical, Physical and Engineering Sciences*, 1982. https://doi.org/10.1098/rspa.1982.0126.

[19] Abaqus, "Analysis user's guide," Tech. rep., Dassault Systemes Simulia Corp., Providence, Rhode Island, 2014.

[20] Jules, T., Lechenault, F., and Adda-Bedia, M., "Local mechanical description of an elastic fold," *Soft Matter*, 2019. https://doi.org/10.1039/c8sm01791c.

[21] Sedykh, V. D., "Four vertices of a convex space curve," *Bulletin of the London Mathematical Society*, 1994. https://doi.org/10.1112/blms/26.2.177.